Article

Not peer-reviewed version

Large-Scale Fabrication of Tunable Sandwich-structured Silver Nanowires/Aramid Nanofiber Films for Exceptional Electromagnetic Interference (EMI) Shielding

Xinbo Jiang , Guoqiang Cai , Jiangxiao Song , Yan Zhang * , Bin Yu , Shimin Zhai , Kai Chen , Hao Zhang , Yihao Yu , Dongming Qi *

Posted Date: 22 November 2023

doi: 10.20944/preprints202311.1332.v1

Keywords: EMI shielding; sandwich structure; aramid nanofibers; environmental suitability

Article

Large-Scale Fabrication of Tunable Sandwich-structured Silver Nanowires/Aramid Nanofiber Films for Exceptional Electromagnetic Interference (EMI) Shielding

Xinbo Jiang [1], Guoqiang Cai [2], Jiangxiao Song [1], Yan Zhang [1,3,4,*], Bin Yu [5], Shimin Zhai [1,3,4], Kai Chen [1,3,4], Hao Zhang [1], Yihao Yu [6] and Dongming Qi [1,3,4,*]

[1] Key Laboratory of Advanced Textile Materials and Manufacturing Technology and Engineering Research Center for Eco-Dyeing & Finishing of Textiles, Zhejiang Sci-Tech University, Hangzhou, Zhejiang 310018, People's Republic of China
[2] Nice Zhejiang Technology Co., Ltd., Hangzhou, Zhejiang 310018, People's Republic of China
[3] Key Laboratory of Green Cleaning Technology & Detergent of Zhejiang Province, Lishui, Zhejiang 323000, People's Republic of China
[4] Shaoxing-Keqiao Institute, Zhejiang Sci-Tech University, Shaoxing, Zhejiang 312000, People's Republic of China
[5] State Key Laboratory of Fire Science, University of Science and Technology of China, 96 Jinzhai Road, Hefei, Anhui 230026, People's Republic of China
[6] Zhejiang King Label Technology Co., Ltd., Huzhou, Zhejiang 313100, People's Republic of China
* Correspondence: Fax/Tel: +86-0571-86843707; E-mail address: zy52360@zstu.edu.cn (Yan Zhang); *Corresponding author. Fax/Tel: +86-0571-86843707; E-mail address: dongmingqi@zstu.edu.cn (Dongming Qi)

Abstract: The recent advancements in communication technology have facilitated the widespread deployment of electronic communication equipment globally, resulting in the pervasive presence of electromagnetic pollution. Consequently, there is an urgent necessity to develop a thin, lightweight, efficient, and durable electromagnetic interference (EMI) shielding material, capable of withstanding severe environmental conditions, and possessing a scalable production method. In this paper, we proposed an innovative and scalable method for preparing EMI shielding films with a tunable sandwich-structure. The film possesses a nylon mesh (NM) backbone, with AgNWs serving as the shielding coating and aramid nanofibers (ANFs) acting as the cladding layer. The prepared film was thin and flexible, with a thickness of only 0.13 mm. AgNWs could easily form a conductive network structure with excellent performance, and the film had a high EMI shielding efficiency, up to 50.6 dB with 1.0mg/cm^2. Due to the outstanding thermal resistance, acid and alkali resistance properties of aramid fibers, the NAAANF film demonstrates remarkable robustness in the face of complex usage environments. Such a thin, efficient and environmentally resistant EMI shielding film provided new ideas for the broad EMI shielding market.

Keywords: EMI shielding; sandwich structure; aramid nanofibers; environmental suitability

1. Introduction

With the rapid development of communication technology and the widespread deployment of public mobile communication base stations, electronic signals now cover a vast majority of areas [1–5]. However, the resulting EM pollution brings about a host of problems that seriously affect both human health and the normal operation of high-precision electronic equipment [6–8]. To address these issues, lightweight and flexible EMI shielding films have gained extensive application in the field of intensive and lightweight electronic devices [9–12]. Nevertheless, current challenges faced by EMI shielding films also include low shielding efficiency, inadequate mechanical properties, and

 doi:10.20944/preprints202311.1332.v1

difficulties in large-scale production, which significantly restrict their application and development [13,14]. Therefore, there is an urgent need for the development of multifunctional EMI shielding films that are lightweight, flexible, highly effective and rapidly producible.

The thickness of EMI shielding materials is positively correlated with their shielding properties, making the improvement of EMI shielding film efficiency a key focus in research [15–18]. In order to address this issue, researchers have conducted a diverse range of investigations, primarily focusing on the utilization of multi-layer structures, "brick-mortar" structures, aerogel structures, asymmetric structures, sandwich structures and other related approaches [19–21]. For example, Li et al. fabricated flexible and tough nanofibrillated cellulose/Fe_3O_4 and carbon nanotube/polyethylene films with multilayer alternating structures using an alternate vacuum-assisted filtration technique, which demonstrated an electromagnetic interference shielding effectiveness (EMI SE) value of 30.3 dB [22]. Inspired by the structure of "brick and mortar," Gong et al. fabricated a multifunctional flexible composite membrane composed of PCC/MXene/polyvinyl alcohol (PMP) using a one-step vacuum-assisted filtration method, exhibiting an EMI SE value of 43.13 dB [23]. Besides, Fu et al. proposed a laminated structural engineering strategy for the fabrication of an autonomous carbon nanotube-based aerogel film, which exhibits a compacted porous structure contributing to an enhanced EMI SE value of 35.1 dB through effective internal reflection loss [16]. Among the aforementioned methods, sandwich-structured EMI shielding films can establish conductive networks by concentrating electrically/magnetically conductive fillers in specific layers. Therefore, the sandwich structure not only effectively enhances EMI shielding efficiency, but also provides structural support to the entire film and safeguards the intermediate shielding filler against friction, oxidation, and other forms of damage. As reported, Yao et al. prepared sandwich-structured $Ti_3C_2T_x$ MXene/ANF films with an EMI SE greater than 49.7 dB by using a layer-by-layer construction method [24]. However, at present, the preparation of sandwich-structured films through vacuum filtration is highly inefficient, necessitating the urgent development of a rapid and large-scale film fabrication method.

The incorporation of a high-performance polymer with exceptional mechanical properties and an effective shielding filler represents a viable approach to enhance the mechanical characteristics of EMI shielding composite films [25–27]. Aramid fiber is a such kind of high performance polymer fiber which has been widely studied and developed in recent decades [28–31]. It is known for its excellent strength, high modulus and high heat resistance, [32] and since Takayanagi et al. discovered the solubility of aramid, researchers have found a simple preparation method for aramid nanofibers (ANFs) [33]. ANFs are extracted from macro aramid fibers by chemical etching and stripping, which is very simple and fast at present [34–36]. ANFs inherit the excellent mechanical properties and thermal stability of macro aramid fibers. Wang et al. constructed a bidirectional conductive network to prepare a dual-function thermal management material. The film has a thermal stability of 31.3 W/mK and a mechanical strength of more than 100 MPa [37]. At the same time, at the nano and micro level, it can be easily prepared into a film, which has become a basic building unit of high-performance composite materials and attracted our strong attention. For example Wang et al. added ND@PDDA to ANF/DMSO blending and scraped protonation film, which is of great significance for practical engineering applications [38]. Zhou et al., prepared ANF@PPy thin films with an EMI SE of 41.69 dB when the amount of pyrrole (Py) monomer was 40 uL [39]. In addition, among various EMI shielding fillers, silver nanowires with one-dimensional structure and high aspect ratio have ultra-high electrical conductivity up to 6.3×10^7 S/m. Therefore it is easy to construct excellent two-dimensional conductive network structures and obtain excellent flexibility, which can be widely used in EMI shielding films. For example, Zeng et al. prepared WPU/AgNWs nanocomposites with unidirectionally aligned micrometer-sized pores, where only 28.6 wt% of AgNWs could reach up to 64 dB in the X-band [40].

In this work, the ANFs were prepared by dissolving aramid fibers in an alkaline solution of dimethyl sulfoxide using the aramid deprotonation method. Subsequently, a NM was utilized as a scaffold onto which the ANFs solution was applied and subsequently water-bathed, resulting in the formation of an aramid nanofiber film (ANF) supported by the scaffold. To create a conductive network structure with excellent EMI shielding properties, AgNWs solution was sprayed onto the

 doi:10.20944/preprints202311.1332.v1

surface of the film. Furthermore, to form a sandwich structure, another coating scraping step of ANFs solution was repeated to encapsulate the AgNWs conductive network structure inside. This sandwich-structured film allows for controllable EMI shielding efficiency by adjusting the loading amount of AgNWs. Additionally, due to its inner NM skeleton and outer ANF coatings, this film exhibits exceptional mechanical properties and thermal stability. Our work holds significant implications for facilitating rapid industrialized production of high-performance EMI shielding films.

2. Experimental Section

2.1. Chemicals and Materials

Poly-paraphenylene terephthalamide (PPTA) were bought from Yantai Tayho Advanced Materials Group Co., Ltd., China. Nylon mesh (NM, 200 mesh) were provided by Changzhou Hongli Hardware Co., LTD, China. Dimethyl sulfoxide (DMSO), potassium hydroxide (KOH), polyvinyl pyrrolidone (PVP, Mw≈5,8000) and glycerol were all purchased from Shanghai Aladdin Biochemical Technology Co., Ltd., China. Silver nitrate ($AgNO_3$) is supplied by Guangdong Guanghua Sci-Tech Co., Ltd., China. Sodium chloride (NaCl) is supplied by Tianjin baishi Chemical Industry Co., Ltd., China. Deionized water (DI water) is supplied by minling material. All chemicals were used without further purification.

2.2. Preparation of AgNWs

The AgNWs were synthesized using the well-established polyol reduction method [41,42]. 190 mL of glycerol and 5.86 g of PVP were added to a 250 mL three-necked flask, followed by gradual heating from room temperature to 80 °C at a lower rotational speed. The temperature was then maintained between 80 and 90 °C until complete dissolution of PVP was achieved. Subsequently, the solution was allowed to cool down after discontinuing the heating process. Meanwhile, a mixture of 0.059 g of NaCl in 500 μL of DI water and 10 mL of glycerol was prepared by homogeneous mixing and preheated at 60 °C for at least 5 minutes. Once the PVP-propanetriol solution reached a temperature of 55 °C, it was supplemented with 1.58 g of $AgNO_3$ followed by addition of the preheated NaCl mixture. The whole reaction system was gradually heated up to 210 °C with a lower stirring speed and then the heating was stopped. The gray-green product was taken out, cooled to room temperature and then a large amount of DI water was added and stand for one week. After that, the mixture underwent three rounds of centrifugation at 4000 rpm using DI water as the washing agent. Ultimately, the AgNWs were dispersed in ethanol to yield an AgNWs solution.

2.3. Preparation of ANFs/DMSO Solution

The ANFs were prepared by the previously reported deprotonation process [33,43,44]. Specifically, 1 g of KOH was dissolved in the mixed solvent containing 2 mL of DI water and 100 mL of DMSO. Then 1 g of PPTA was added. After stirring for 4 hours at room temperature, a dark red viscous ANFs/DMSO solution was obtained with a concentration of 10 mg/mL.

2.4. Preparation of NAAANF Films

The preparation process of NAAANF was illustrated in Scheme 1a. The entire experiment was carried out at room temperature. Firstly, the ANFs/DMSO solution was coated on NM (Scheme 1b), and then the complete film was immediately immersed in water for 5 minutes to ensure thorough protonation of ANFs. In this process, the reddish-brown film will gradually become transparent, which means that ANFs protonation was complete and formed a cross-linked ANF. Subsequently the wet film was dried at 60 °C for 30 minutes in a oven, resulting in the formation of NANF (Scheme 1c). The inner EMI shielding layer was prepared by spraying the required amount of AgNWs on the NANF surface, and the film was denoted as NAANF (Scheme 1d). Finally, the above steps were repeated to prepare another layer of ANF on the AgNWs coating to obtain NAAANF EMI shielding

Preprints (www.preprints.org) | NOT PEER-REVIEWED | Posted: 22 November 2023 doi:10.20944/preprints202311.1332.v1

film (Scheme 1e). These films were labeled as NAAANF0.2, NAAANF0.4, NAAANF0.6, NAAANF0.8 and NAAANF1.0 based on the amount of AgNWs added (ranging from 0.2 to 1.0 mg/cm^2).

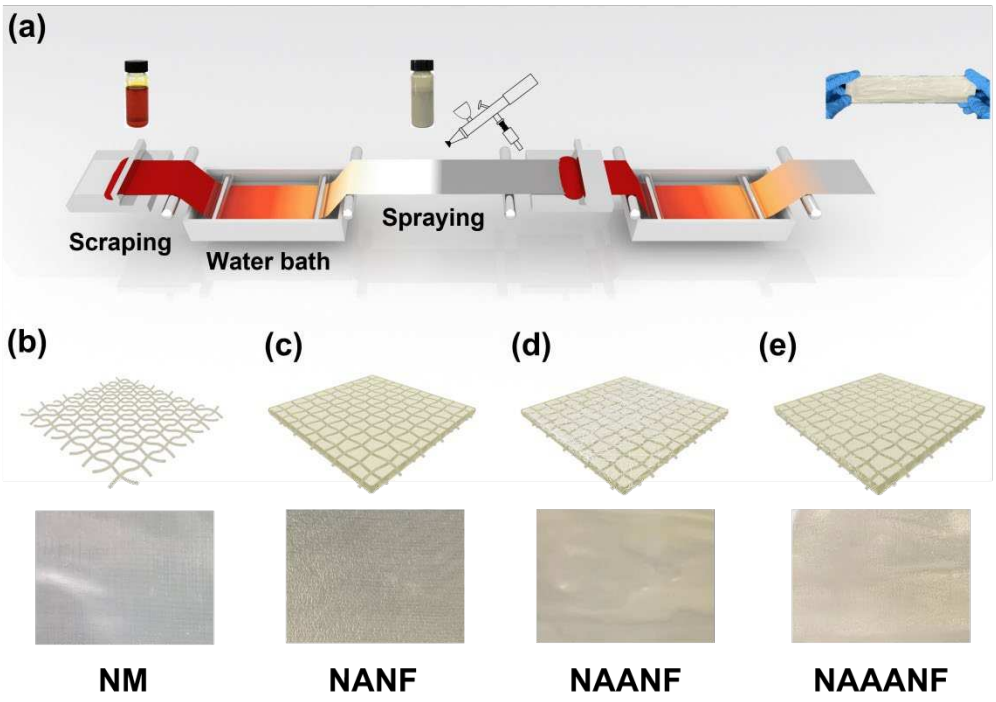

Scheme 1. (**a**) The preparation process of NAAANF. Schematic structure and digital picture of (**b**) NM, (**c**) NANF, (**d**) NAANF, (**e**) NAAANF.

2.5. Characterizations

The morphology and microstructure of AgNWs, ANFs, NANF, NAANF, and NAAANF were observed by field emission scanning electron microscopy (SEM, GeminiSEM500, Zeiss). The sample was sprayed with gold for 5 minutes prior to testing and the acceleration voltage during the test was 3 kV. Microscopic morphology of the raw materials ANFs and AgNWs was observed using transmission electron microscopy (TEM, JEM-1400Flash, JEOL) at an acceleration voltage of 120 kV. X-ray diffraction (XRD, D8 Advance, Bruker-AXS) of the sample used a copper target with diffraction angles ranging from 5 to 90°. Thermogravimetric analysis (TGA, TG209F1, NETZSCH) was used to analyze the thermal stability of the samples. The analysis was conducted in a nitrogen atmosphere, with a temperature range from 25 to 800 °C and a heating rate of 10 °C/min. A four-finger probe tester (FT-340, CHNT) was used to measure the resistance of different AgNWs concentrations. The EMI SE properties of the composite in the 8-12 GHz (X-band) microwave range were measured by waveguide method using vector network analyzer (VNA, AV3672, Ceyear). The measured scattering parameters (S11 and S21) were used to calculate the EMI SE of the materials, from which the total EMI SE (SE_T), absorbing shielding effectiveness (SE_A), reflecting shielding effectiveness (SE_R), and power coefficients of absorptivity (A), reflectivity (R), and transmittance (T) were calculated as follow:

$R = |S11|^2$

$T = |S21|^2$

$1 = A + R + T$

$SE_R = -10 \log (1 - R)$

$SE_A = -10 \log (T/(1 - R))$

$SE_T = SE_A + SE_R + SE_M$

The multiple reflection (SE_M) was generally ignored when $SE_T > 15$ dB [45]. Tensile stress and strain test was performed on a universal testing machine (KJ-1065B, Kejian) at a speed of 10 mm/min to test the strip sample of 10 cm×1 cm [46].

Preprints (www.preprints.org) | NOT PEER-REVIEWED | Posted: 22 November 2023 doi:10.20944/preprints202311.1332.v1

3. Results and Discussion

3.1. Morphologies and Microstructures of ANFs and AgNWs

The purchased PPTA (Figure 1a) was dissolved in a KOH/DMSO solution to obtain ANFs/DMSO solution (Figure 1b), which was then added to DI water and dispersed using ultrasonication to obtain an ANFs dispersion solution (Figure 1c). In order to confirm the successful preparation of ANFs, the ANFs was characterized by SEM (Figure 1d) and TEM (Figure 1e). The SEM image revealed one-dimensional fiber-like structure of ANFs with diameters ranging from 20-30 nm. Additionally, Figure 1f is a comparison of the XRD patterns of ANFs and PPTA. Diffraction peaks at 20.6°, 23.0°, 28.7°, and 39.1° appeared for PPTA, which corresponded to the (110), (200), (004), and (006) crystal faces of PPTA. While the XRD spectra of ANFs were almost flattened, which suggested that the crystal structure of PPTA was disrupted by deprotonation of ANFs, further indicating the formation of ANFs. To assess whether the thermodynamic properties were retained during the conversion from PPTA to ANFs, TGA and DTG curves were performed under a nitrogen atmosphere. The results indicated that both PPTA and ANFs exhibites weight loss at temperatures above 500 °C, suggesting that deprotonated ANFs still possessed high thermal stability.

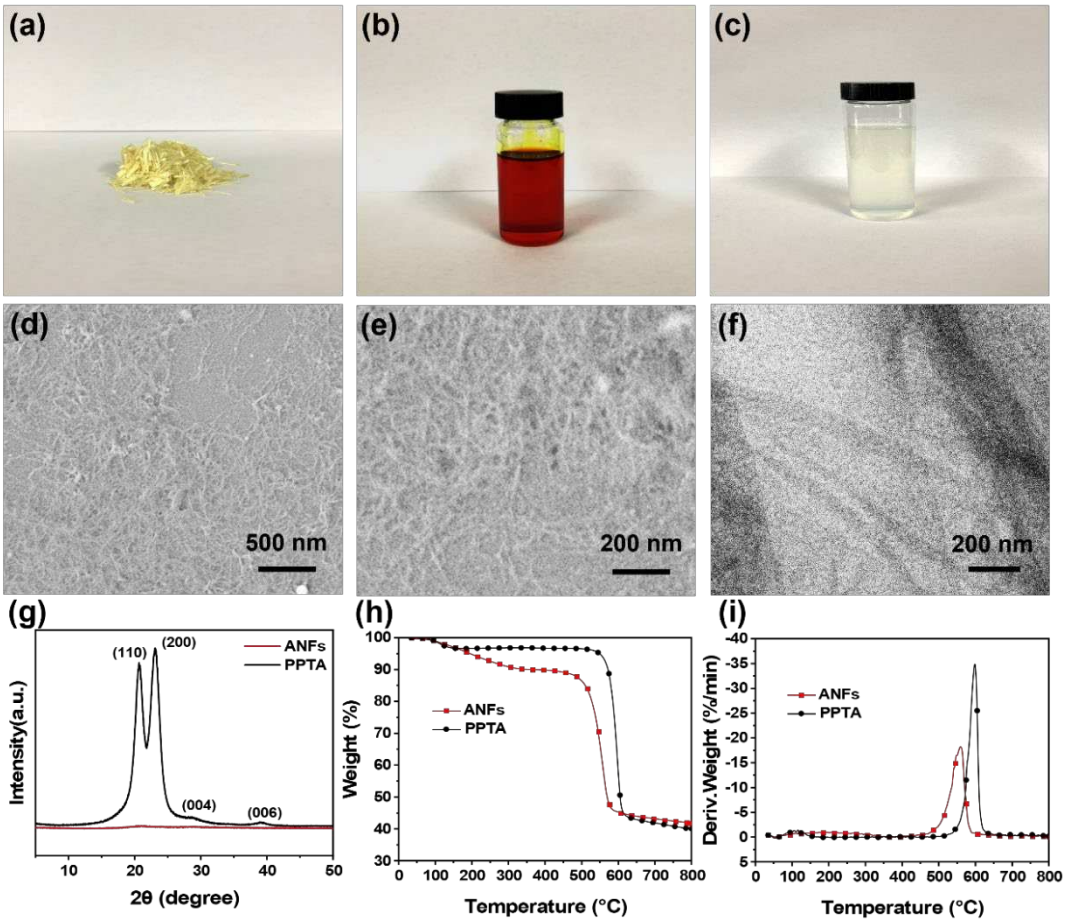

Figure 1. (**a**) PPTA, (**b**) ANFs/DMSO solution and (**c**) ANFs solution. (**d**) SEM image and (**e**) TEM image of ANFs, (**f**) XRD of ANFs and PPTA, (**g**) TGA and (**h**) DTG curves of ANFs and PPTA.

Table 1. TGA related parameters of ANF and PPTA.

Sample	$T_{-5wt\%}$ (°C)	T_{max} (°C)	Residue at 800 °C (wt %)
ANF	195	560	40.6
PPTA	548	598	39.7

Preprints (www.preprints.org) | NOT PEER-REVIEWED | Posted: 22 November 2023 doi:10.20944/preprints202311.1332.v1

AgNWs was simply synthesized by polyol reduction method and uniformly dispersed in anhydrous ethanol (Figure 2a). The AgNWs dispersion liquid exhibited a silver-gray color with a slight green tint. SEM analysis revealed the microstructure of the prepared AgNWs, as shown in Figure 2b, and TEM analysis further confirmed their characteristics, as depicted in Figure 2c. It was observed that the length of the AgNWs was approximately 20 μm, with a diameter less than 100 nm and a length-to-length ratio exceeding 200. Some slightly curved AgNWs observed in SEM indicated their inherent flexibility, making them suitable for applications in flexible film materials. Diffraction peaks at 38.1 °, 44.2 °, 64.3 °and 77.4 ° appeared in the XRD (Figure 2d) patters. The peaks can be respectively designated as (111), (200), (220) and (311) facets, all in excellent accordance with the faced-centered cubic (FCC) Ag crystal nanostructure.

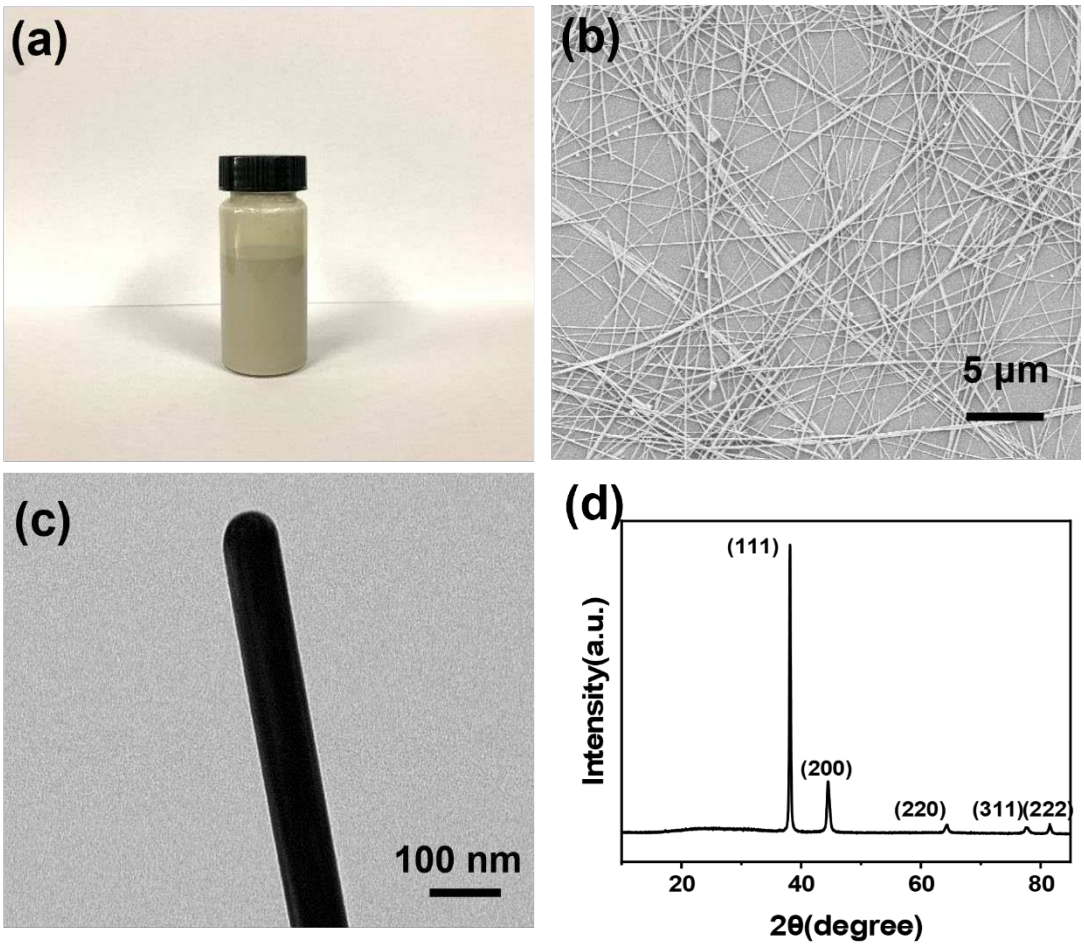

Figure 2. (**a**) AgNWs solution. (**b**) SEM image, (**c**) TEM image and (**d**) XRD of AgNWs.

3.2. Structurale Characterization of NAAANF

Scheme 1a illustrated the fabrication process of the NAAANF composite films. The colorless and translucent 200-mesh NM yarn with warp and weft interlacing (Figure 3a) demonstrates a certain level of mechanical strength. Owing to the utilization of NM as a foundation, the ANFs/DMSO solution was meticulously coated onto NM via a blade process, followed by protonation to generate a functional membrane. The SEM image of NANF was shown in Figure 3b. It appeared light yellow and semi-transparent (Scheme 1c), resembling a leaf, where NM acted as the leaf veins and ANF as the leaf blade. Subsequently, various amount of AgNWs were sprayed onto the NANF surface to form a conductive network structure. NAANF had the same metallic luster as the AgNWs we synthesized (Scheme 1d). SEM images of NAANF with different AgNWs concentrations were shown in Figure 3c-3g. NAANF0.2 (Figure 3c) containing 0.2 mg/cm² of AgNWs exhibits significant spacing in the conductive network, which becomes tighter as the content of AgNWs increases. Especially, the saturation point was reached at 0.8 mg/cm² of AgNWs deposited by spraying on NANF, which was

Preprints (www.preprints.org) | NOT PEER-REVIEWED | Posted: 22 November 2023 doi:10.20944/preprints202311.1332.v1

particularly evident in NAANF1.0. Finally, to protect the exposed AgNWs conductive network, the scraping and protonation steps described above were repeated on the NAANF. The AgNWs were completely enveloped by the final layer of ANF, resulting in the formation of a sandwich structure composed of ANF-AgNWs-ANF. The preparation of NAAANF was successfully completed. The final NAAANF was in a grayish-yellow film state (Scheme 1e). The SEM image in Figure 3h illustrates the encapsulation of AgNWs by the final layer of ANF film, providing effective protection against detachment and oxidation.

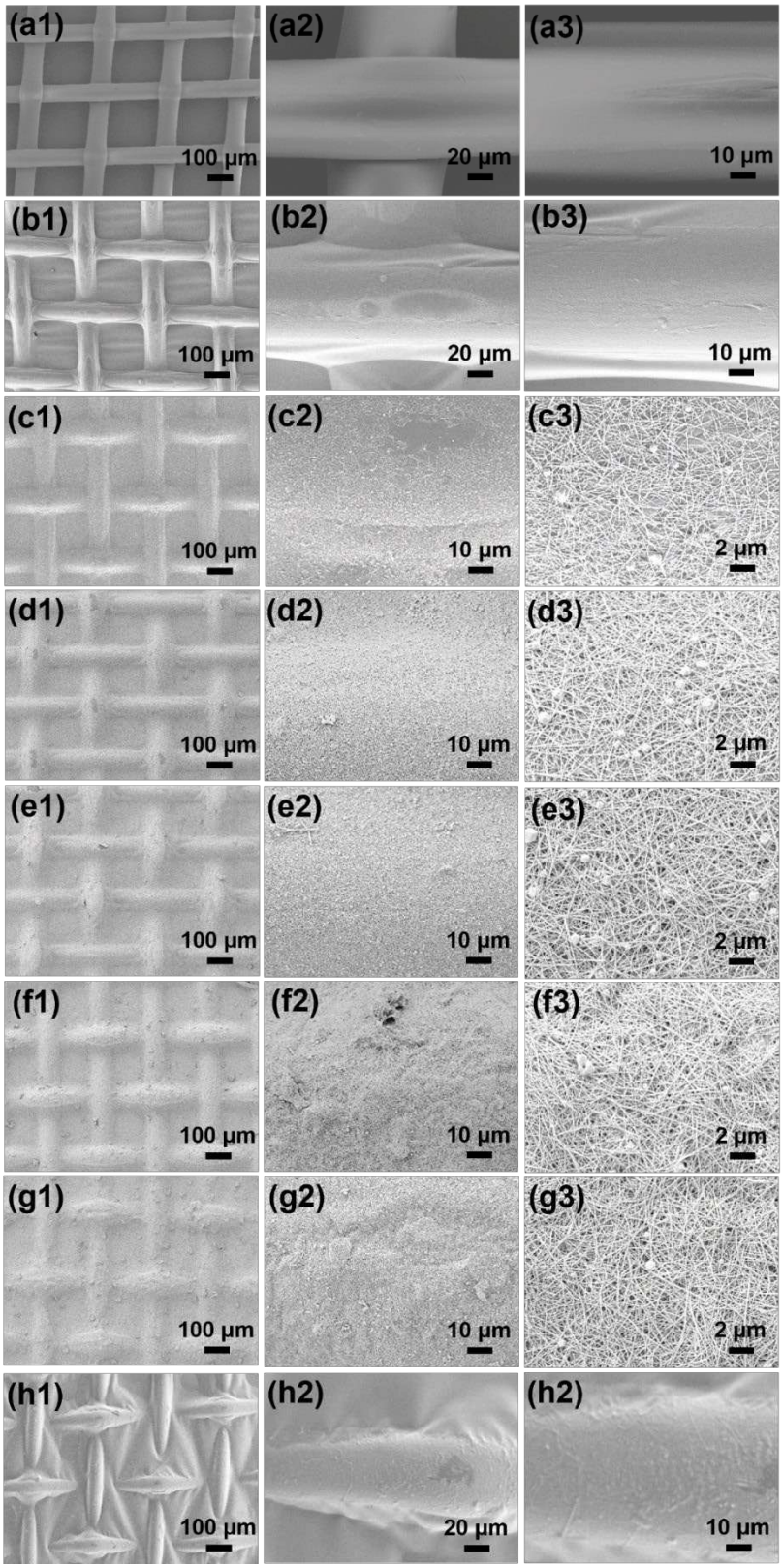

Preprints (www.preprints.org) | NOT PEER-REVIEWED | Posted: 22 November 2023 doi:10.20944/preprints202311.1332.v1

Figure 3. SEM image of the NM (**a1**,**a2**,**a3**), NANF (**b1**,**b2**,**b3**), NAANF0.2 (**c1**,**c2**,**c3**), NAANF0.4 (**d1**,**d2**,**d3**), NAANF0.6 (**e1**,**e2**,**e3**), NAANF0.8 (**f1**,**f2**,**f3**), NAANF1.0 (**g1**,**g2**,**g3**) and NAAANF (**h1**,**h2**,**h3**).

3.3. Electrical Conductivity and EMI shielding Properties of NAAANF

Electric and magnetic fields interact with each other to form EM waves, which propagate in a manner similar to sound waves. These waves undergo changes when they transition from one medium to another. EM waves encountered impedance mismatch and produced numerous reflections when interacting with conductive materials in different media. Materials with better conductivity are more likely to cause impedance mismatch, thus their shielding performance is relatively superior. Figure 4a showed the surface resistance of the NAAANF films with different loading amounts of AgNWs. As the AgNWs content increased, the surface resistance of the film decreased, with the NAAANF1.0 sample exhibiting having had a resistance of only 0.58 Ω. Additionally, Figure 4b depicted the construction of a conductive channel for a small light bulb, which visualized the different conductive properties of the NAAANF films. When an applied voltage of 3 V was utilized, the brightness of the light bulb was found to increase with the concentration of AgNWs in the film.

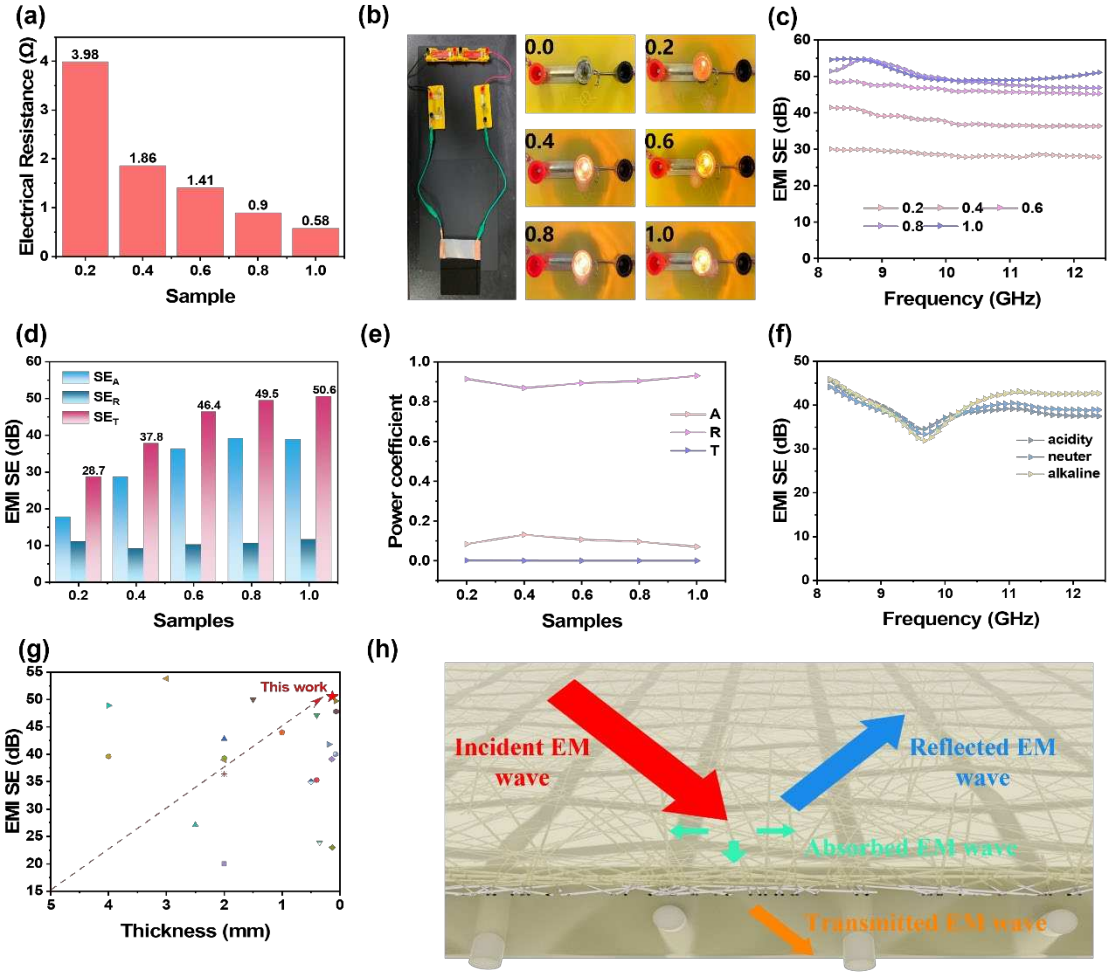

Figure 4. (**a**) Surface resistance of NAAANF, (**b**) Electrical conductivity of NAAANF is demonstrated by small light bulbs, (**c**) EMI shielding performance at the X-band, (**d**) average EMI SE_T, SE_A, and SE_R values, and (**e**) power coefficients of reflectivity (R) and absorptivity (A) values of NAAANF, (**f**) NAAANF0.4 EMI performance after 48h immersion in acidic, alkaline, and DI water, (**g**) This work compares with other recent studies on thickness and EMI performance, (**h**) Schematic of electromagnetic shielding mechanism.

Preprints (www.preprints.org) | NOT PEER-REVIEWED | Posted: 22 November 2023 doi:10.20944/preprints202311.1332.v1

Due to the high conductivity of the AgNWs coating in NAAANF films, significant impedance mismatch and substantial conduction losses occurred when exposed to EM waves, making them highly efficient in EMI shielding. To evaluate their performance, we evaluated the EMI SE in the frequency range of 8.2-12.4 GHz (X-band). As anticipated, a direct correlation between the conductivity trends and the EMI SE enhancements of the NAAANF films was observed, as depicted in Figure 4c. Remarkably, the NAAANF0.2 sample displayed an average EMI SE of 28.6 dB, indicating its ability to attenuate 99.884% of incident EM waves, surpassing the requirements for commercial EMI shielding (20 dB). Subsequently, the NAAANF0.4, NAAANF0.6, NAAANF0.8, and NAAANF1.0 samples exhibited progressively increasing average EMI SE values of 37.7 dB, 46.4 dB, 49.5 dB, and 50.6 dB, respectively. Notably, the EMI SE improvement from NAAANF0.8 to NAAANF1.0 was marginal, suggesting that the EMI shielding effectiveness reached a saturation point at an AgNWs concentration of 0.8 mg/cm^2. This observation further substantiated our previous analysis, indicating that the maximum EMI shielding performance was attained when the conductive plane of the NAAANF film was fully covered and reached saturation.

The shielding mechanisms of EMI shielding materials included reflection, absorption, and multiple reflection. To elucidate the EMI shielding mechanism of NAAANF, we calculated the EMI shielding effects in terms of EMI SE_T, EMI SE_R, and EMI SE_A, and the corresponding coefficients T, R, and A, as shown in Figure 4d and 4e. Nevertheless, the basic principle of EM wave propagation had to be taken into account. When an EM wave encountered an EMI shielding material in an air medium, an initial impedance mismatch triggered a large reflection, which then partially penetrated the material and was subsequently absorbed through dielectric losses. It was noteworthy that the SE_A values for the NAAANF series surpassed their respective SE_R values. Did this suggest that NAAANF had potent absorption properties concerning EMI shielding? Considering the fundamental principle of EMI shielding, when an EM wave met an EMI shielding material in an air medium, an initial impedance mismatch caused a substantial reflection. Subsequently, part of the wave penetrated the material and underwent absorption due to dielectric loss. An analysis of the SE_R values across the entire film revealed that over 90% of the incident EM wave was efficiently reflected upon interacting with NAAANF. Furthermore, the coefficients R and A offered additional insights. Notably, the R value significantly outpaced the A value, reinforcing the notion that the NAAANF series primarily functioned as a reflective EMI shielding material.

NAAANF films were often exposed to complex and harsh environmental climates during actual use. The most important thing was that the upper and lower layers of ANF protected the AgNWs conductive layer. We needed to test in the extreme environment after treatment of NAAANF film to see if it could maintain better EMI shielding performance. As shown in Figure 4f, the sample NAAANF0.4 had been soaked in acidic solution (pH=2), alkaline solution (pH=13), and DI water (pH=7) for 48 hours and was then dried. The curves of the samples treated under the three conditions fluctuated slightly, but their EMI shielding performance remained very good, with average EMI SE values of 38.6, 38.7, and 40.2 dB, respectively. This fully demonstrated that the ANF film was resistant to acid and alkali, and effectively protected the conductive network structure of the AgNWs from damage. The experiment proved that the EMI film had excellent environmental performance. Figure 4g showed the thickness and EMI shielding performance of this work compared to other recent studies. The sample in this work achieved very excellent EMI shielding performance under extremely thin conditions, allowing it to be applied in more extreme environments. Figure 4h showed the structure and EMI shielding mechanism of the NAAANF. A high impedance mismatch occurred when the incident EM wave reached the surface of the thin film and the highly conductive network composed of AgNWs. Therefore, 90% of the EM wave was reflected, a small amount of the EM wave was polarized and dissipated as heat in the conductive network, and a small amount of the EM wave passed through the film.

3.4. Mechanical Properties and Thermal Stability of NAAANF

Basic mechanical properties needed to be taken into account for thin film material applications. The NM used in this film had good basic mechanical properties, and it was expected that the scratch

Preprints (www.preprints.org) | NOT PEER-REVIEWED | Posted: 22 November 2023 doi:10.20944/preprints202311.1332.v1

coating addition of ANF would further enhance the mechanical properties of NAAANF. Figures 5a and 5b illustrated typical stress-strain plots for NM, NANF, and NAAANF films along with the corresponding tensile strength and elongation. As the NM served as the supporting framework for the film, during external tensile fracturing, certain yarns within the NM underwent initial rupture due to uneven stress distribution. From the stress-strain curve, this characteristic was reflected as a step-wise fracture behavior in the deformation stage of NM and NANF. In terms of mechanical strength, NANF demonstrated a slight enhancement compared to NM, with the tensile strength increment from 35.7 MPa to 38.6 MPa, and the strain increase from 85.4% to 75.5% at the point of fracture initiation. However, owing to the thicker ANF coating resulted from the deposition of two ANFs, NAAANF films exhibited increased interconnectivity among the ANFs, which significantly affects the manifestation of the stress-strain curve for the thin film. Notably, NAAANF films displayed a single distinct fracture point, in contrast to the multiple fracture points observed in NM and NANF, indicative of the uniform distribution of external forces facilitated by ANFs. Among the NAAANF series samples, NAAANF0.2 and NAAANF0.4 demonstrated favorable tensile strength, reaching 50 MPa. NAAANF0.6 showed a slight decline, while NAAANF0.8 and NAAANF1.0 exhibited tensile strengths approximately at 40 MPa, similar to that of NANF. Overall, the strain level for NAAANF resided around 29%, highlighting its superior overall structural integrity compared to NM and NANF.

Figure 5c,d depicted the TGA and DTG curves, respectively, for NM, NANF and NAAANF under a nitrogen atmosphere. Additionally, Table 2 presented the corresponding data in detail. Analysis of the figures revealed that the degradation of the samples occurs after 390 °C, indicative of the favorable thermal stability exhibited by NM. The addition of AgNWs and ANF in NANF and NAAANF did not affect the overall thermal degradation trend, but resulted in a slightly higher residual carbon content compared to NM.

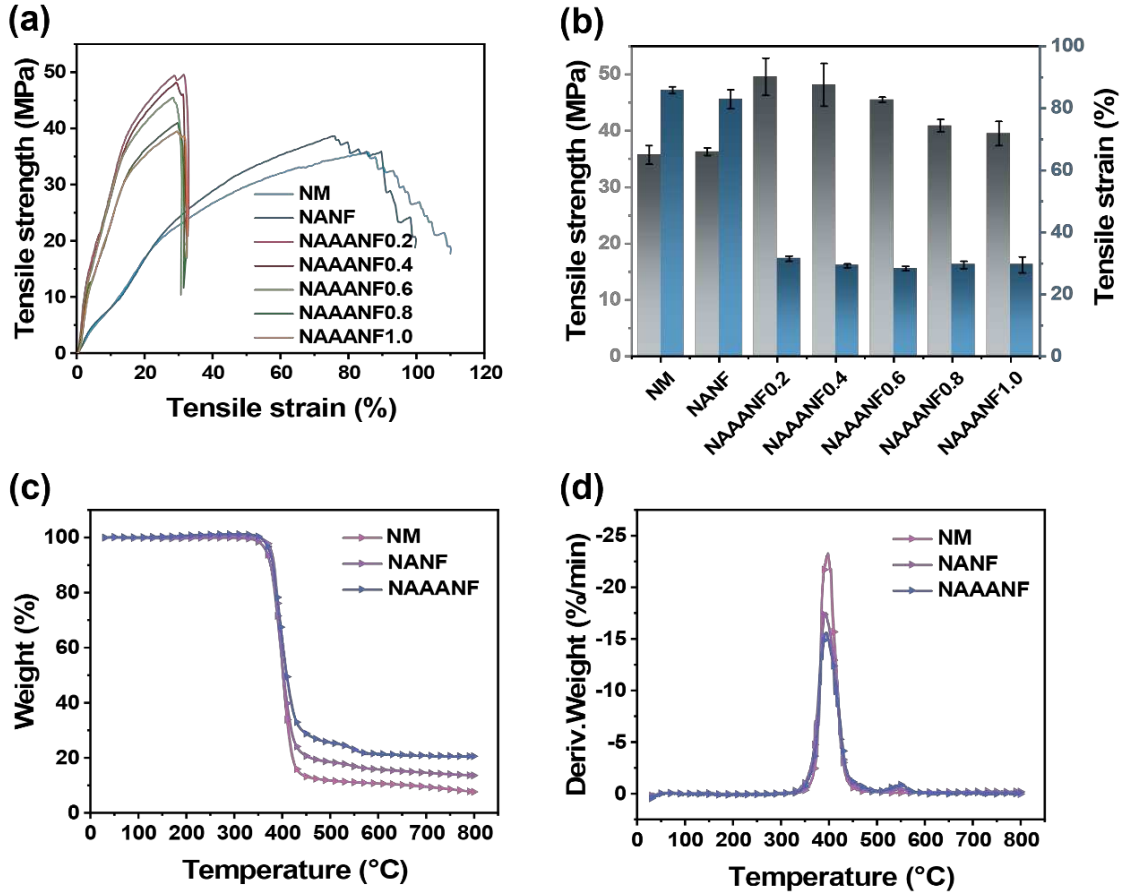

Figure 5. (**a**) tensile strength–tensile strain curves, (**b**) tensile strength and tensile strain of NM, NANF and NAAANF, (**c**) TGA and (**d**) DTG curves of NM, NANF and NAAANF.

Table 2. TGA related parameters of NM, NANF and NAAANF.

Sample	$T_{-5wt\%}$ (°C)	T_{max1} (°C)	Residue at 800 °C (wt %)
NM	387.4	398.0	7.64
NANF	366.9	393.9	13.59
NAAANF	373.7	393.8	20.57

4. Conclusions

Based on the aforementioned statement, we successfully fabricated a flexible, high-performance EMI shielding film that offered rapid preparation and adaptability to various environmental conditions. We used a scratch-coating ANFs and spray-coating AgNWs method to prepare sandwich-structured NAAANF films. This method is cleverly designed and allows for the rapid preparation of ultra-thin electromagnetic shielding films. The addition of 1.0 mg/cm^2 AgNWs resulted in a shielding effectiveness of up to 50.6 dB. Furthermore, the film was subjected to extreme acidic and alkaline environments, yet its electromagnetic shielding performance remained excellent. Our research contributed novel insights to the domain of ultra-thin, high-performance EMI shielding films. The simplicity of operation and cost-effectiveness made this film particularly promising for widespread utilization in the realm of electronic devices.

Acknowledgments: The work was financially supported by the National Natural Science Foundation of China (No. 52203105), Zhejiang Provincial Natural Science Foundation (No. LQ22E030007), Zhejiang Provincial Key Research and Development Program (No. 2022C01174 and 2023C01202), National innovation and Entrepreneurship training program for college students (No. 202210338016) and Science Foundation of Zhejiang Sci-Tech University (ZSTU) (No. 2020YBZX24 and 20202291-Y).

References

1. Xie, Y.; Liu, S.; Huang, K.; Chen, B.; Shi, P.; Chen, Z.; Liu, B.; Liu, K.; Wu, Z.; Chen, K.; et al. Ultra-Broadband Strong Electromagnetic Interference Shielding with Ferromagnetic Graphene Quartz Fabric. *Adv. Mater.* **2022**, *34*, 2202982. https://doi.org/10.1002/ADMA.202202982.
2. Rebecchi, F.; Pastor, A.; Mozo, A.; Lombardo, C.; Bruschi, R.; Aliferis, I.; Doriguzzi-Corin, R.; Gouvas, P.; Alvarez Romero, A.; Angelogianni, A.; et al. A Digital Twin for the 5G Era: The SPIDER Cyber Range. *2022 IEEE 23rd Int. Symp. a World Wireless, Mob. Multimed. Networks* **2022**. https://doi.org/10.1109/WoWMoM54355.2022.00088.
3. Wang, J.; Wu, X.; Wang, Y.; Zhao, W.; Zhao, Y.; Zhou, M.; Wu, Y.; Ji, G. Green, Sustainable Architectural Bamboo with High Light Transmission and Excellent Electromagnetic Shielding as a Candidate for Energy-Saving Buildings. *Nano-Micro Lett.* **2023**, *15*, 1–16. https://doi.org/10.1007/S40820-022-00982-7/FIGURES/6.
4. Zhang, Y.; Cheng, W.; Tian, W.; Lu, J.; Song, L.; Liew, K.M.; Wang, B.; Hu, Y. Nacre-Inspired Tunable Electromagnetic Interference Shielding Sandwich Films with Superior Mechanical and Fire-Resistant Protective Performance. *ACS Appl. Mater. Interfaces* **2020**, *12*, 6371–6382. https://doi.org/10.1021/acsami.9b18750.
5. Li, Y.; Shang, Y.; Li, M.; Zhang, X.; He, J. High Electromagnetic Shielding Effect of Carbon Nanotubes/Waterborne Polyurethane Composites Prepared by "Break-Adsorption" Method. *Mater. 2022, Vol. 15, Page 6430* **2022**, *15*, 6430. https://doi.org/10.3390/MA15186430.
6. Abbasi, H.; Antunes, M.; Velasco, J.I. Recent Advances in Carbon-Based Polymer Nanocomposites for Electromagnetic Interference Shielding. *Prog. Mater. Sci.* **2019**, *103*, 319–373. https://doi.org/10.1016/J.PMATSCI.2019.02.003.
7. Shahzad, F.; Alhabeb, M.; Hatter, C.B.; Anasori, B.; Hong, S.M.; Koo, C.M.; Gogotsi, Y. Electromagnetic Interference Shielding with 2D Transition Metal Carbides (MXenes). *Science (80-.).* **2016**, *353*, 1137–1140. https://doi.org/10.1126/SCIENCE.AAG2421/SUPPL_FILE/SHAHZAD.SM.PDF.
8. Cao, C.F.; Yu, B.; Chen, Z.Y.; Qu, Y.X.; Li, Y.T.; Shi, Y.Q.; Ma, Z.W.; Sun, F.N.; Pan, Q.H.; Tang, L.C.; et al. Fire Intumescent, High-Temperature Resistant, Mechanically Flexible Graphene Oxide Network for Exceptional Fire Shielding and Ultra-Fast Fire Warning. *Nano-Micro Lett.* **2022**, *14*, 1–18. https://doi.org/10.1007/S40820-022-00837-1/TABLES/1.
9. Yin, Z.; Lu, J.; Hong, N.; Cheng, W.; Jia, P.; Wang, H.; Hu, W.; Wang, B.; Song, L.; Hu, Y. Functionalizing $Ti_3C_2T_x$ for Enhancing Fire Resistance and Reducing Toxic Gases of Flexible Polyurethane Foam Composites with Reinforced Mechanical Properties. *J. Colloid Interface Sci.* **2022**, *607*, 1300–1312. https://doi.org/10.1016/j.jcis.2021.09.027.

10. Qiu, S.; Zhou, Y.; Zhou, X.; Zhang, T.; Wang, C.; K Yuen, R.K.; Hu, W.; Hu, Y.; Qiu, S.; Zhou, Y.; et al. Air-Stable Polyphosphazene-Functionalized Few-Layer Black Phosphorene for Flame Retardancy of Epoxy Resins. *Small* **2019**, *15*, 1805175. https://doi.org/10.1002/SMLL.201805175.
11. Xiong, J.; Ding, R.; Liu, Z.; Zheng, H.; Li, P.; Chen, Z.; Yan, Q.; Zhao, X.; Xue, F.; Peng, Q.; et al. High-Strength, Super-Tough, and Durable Nacre-Inspired MXene/Heterocyclic Aramid Nanocomposite Films for Electromagnetic Interference Shielding and Thermal Management. *Chem. Eng. J.* **2023**, *474*, 145972. https://doi.org/10.1016/j.cej.2023.145972.
12. Zazoum, B.; Bachri, A.; Nayfeh, J. Functional 2D MXene Inks for Wearable Electronics. *Mater. 2021, Vol. 14, Page 6603* **2021**, *14*, 6603. https://doi.org/10.3390/MA14216603.
13. Pušić, T.; Šaravanja, B.; Malarić, K. Electromagnetic Shielding Properties of Knitted Fabric Made from Polyamide Threads Coated with Silver. *Mater. 2021, Vol. 14, Page 1281* **2021**, *14*, 1281. https://doi.org/10.3390/MA14051281.
14. Liu, H.; Huang, J.; Guo, B.; Liu, H.; Huang, J.; Guo, B. Light Weight, Flexible and Ultrathin PTFE@Ag and Ni@PVDF Composite Film for High-Efficient Electromagnetic Interference Shielding. *Mater. 2023, Vol. 16, Page 4831* **2023**, *16*, 4831. https://doi.org/10.3390/MA16134831.
15. Cheng, M.; Ying, M.; Zhao, R.; Ji, L.; Li, H.; Liu, X.; Zhang, J.; Li, Y.; Dong, X.; Zhang, X. Transparent and Flexible Electromagnetic Interference Shielding Materials by Constructing Sandwich AgNW@MXene/Wood Composites. *ACS Nano* **2022**, *16*, 16996-17007. https://doi.org/10.1021/ACSNANO.2C07111.
16. Fu, C.; Sheng, Z.; Zhang, X. Laminated Structural Engineering Strategy toward Carbon Nanotube-Based Aerogel Films. **2022**, *16*, 9378-9388. https://doi.org/10.1021/acsnano.2c02193.
17. Yu, J.; Cui, Z.; Lu, J.; Zhao, J.; Zhang, Y.; Fan, G.; Liu, S.; He, Y.; Yu, Y.; Qi, D. Integrated Hierarchical Macrostructures of Flexible Basalt Fiber Composites with Tunable Electromagnetic Interference (EMI) Shielding and Rapid Electrothermal Response. *Compos. Part B Eng.* **2021**, *224*, 109193. https://doi.org/10.1016/J.COMPOSITESB.2021.109193.
18. Tretjak, M.; Pralgauskaitė, S.; Matukas, J.; Plyushch, A.; Macutkevič, J.; Banys, J.; Karakashov, B.; Fierro, V.; Celzard, A. Electrical Resistivity and Microwave Properties of Carbon Fiber Felt Composites. *Mater. 2022, Vol. 15, Page 8654* **2022**, *15*, 8654. https://doi.org/10.3390/MA15238654.
19. Yu, B.; Yuen, A.C.Y.; Xu, X.; Zhang, Z.C.; Yang, W.; Lu, H.; Fei, B.; Yeoh, G.H.; Song, P.; Wang, H. Engineering MXene Surface with POSS for Reducing Fire Hazards of Polystyrene with Enhanced Thermal Stability. *J. Hazard. Mater.* **2021**, *401*, 123342. https://doi.org/10.1016/j.jhazmat.2020.123342.
20. Jia, F.; Dong, J.; Dai, X.; Liu, Y.; Wang, H.; Lu, Z. Journal Pre-Proofs Robust, Flexible, and Stable CuNWs/MXene/ANFs Hybrid Film Constructed by Structural Assemble Strategy for Efficient EMI Shielding Robust, Flexible, and Stable CuNWs/MXene/ANFs Hybrid Film Constructed by Structural Assemble Strategy For . *Chem. Eng. J.* **2022**, *452*, 139395. https://doi.org/10.1016/j.cej.2022.139395.
21. Wang, H.; Zhuang, T.; Wang, J.; Sun, X.; Wang, Y.; Li, K.; Dai, X.; Guo, Q.; Li, X.; Chong, D.; et al. Multifunctional Filler-Free PEDOT:PSS Hydrogels with Ultrahigh Electrical Conductivity Induced by Lewis-Acid-Promoted Ion Exchange. *Adv. Mater.* **2023**, 2302919. https://doi.org/10.1002/ADMA.202302919.
22. Li, Y.; Xue, B.; Yang, S.; Cheng, Z.; Xie, L.; Zheng, Q. Flexible Multilayered Films Consisting of Alternating Nanofibrillated Cellulose/Fe_3O_4 and Carbon Nanotube/Polyethylene Oxide Layers for Electromagnetic Interference Shielding. *Chem. Eng. J.* **2021**, *410*, 128356. https://doi.org/10.1016/J.CEJ.2020.128356.
23. Gong, S.; Sheng, X.; Li, X.; Sheng, M.; Wu, H.; Lu, X.; Qu, J. A Multifunctional Flexible Composite Film with Excellent Multi-Source Driven Thermal Management, Electromagnetic Interference Shielding, and Fire Safety Performance, Inspired by a "Brick–Mortar" Sandwich Structure. *Adv. Funct. Mater.* **2022**, *32*, 2200570. https://doi.org/10.1002/ADFM.202200570.
24. Yao, J.; Zhang, L.; Yang, F.; Jiao, Z.; Tao, X.; Yao, Z.; Zheng, Y.; Zhou, J. Superhydrophobic $Ti_3C_2T_x$ MXene/Aramid Nanofiber Films for High-Performance Electromagnetic Interference Shielding in Thermal Environment. *Chem. Eng. J.* **2022**, *446*, 136945. https://doi.org/10.1016/J.CEJ.2022.136945.
25. Yang, B.; Wang, L.; Zhang, M.; Luo, J.; Lu, Z.; Ding, X.; Yang, B.; Wang, L.; Zhang, M.; Luo, J.; et al. Fabrication, Applications, and Prospects of Aramid Nanofiber. *Adv. Funct. Mater.* **2020**, *30*, 2000186. https://doi.org/10.1002/ADFM.202000186.
26. Lee, J.U.; Park, B.; Kim, B.S.; Bae, D.R.; Lee, W. Electrophoretic Deposition of Aramid Nanofibers on Carbon Fibers for Highly Enhanced Interfacial Adhesion at Low Content. *Compos. Part A Appl. Sci. Manuf.* **2016**, *84*, 482–489. https://doi.org/10.1016/J.COMPOSITESA.2016.02.029.
27. Yang, Y.; Huang, C.; Gao, G.; Hu, C.; Luo, L.; Xu, J. Aramid Nanofiber/Bacterial Cellulose Composite Separators for Lithium-Ion Batteries. *Carbohydr. Polym.* **2020**, *247*, 116702. https://doi.org/10.1016/J.CARBPOL.2020.116702.
28. Zhao, B.; Ma, Z.; Sun, Y.; Han, Y.; Gu, J. Flexible and Robust $Ti_3C_2T_x$ /(ANF@FeNi) Composite Films with Outstanding Electromagnetic Interference Shielding and Electrothermal Conversion Performances. **2022**, *3*, 2200162. https://doi.org/10.1002/sstr.202200162.

29. Yixin Han, Kunpeng Ruan, and J.G. Multifunctional Thermally Conductive Composite Films Based on Fungal Tree-like Heterostructured Silver Nanowires@Boron Nitride Nanosheets and Aramid Nanofibers. *Small Struct.* **2022**. https://doi.org/10.1002/anie.202216093.
30. Pan, X.-F.; Yu, G.-H.; Gao, H.-L.; Wang, Z.-Z.; Bao, Z.; Li, X.; Yu, S.-H.; Pan, X.; Yu, G.; Gao, H.; et al. Large-Scale Production of Rectorite Nanosheets and Their Co-Assembly with Aramid Nanofibres for High-Performance Electrical Insulating Nanopapers. *Adv. Mater.* **2022**, 2206855. https://doi.org/10.1002/ADMA.202206855.
31. Yang, B.; Wang, L.; Zhao, J.; Pang, R.; Yuan, B.; Tan, J.; Song, S.; Nie, J.; Zhang, M. A Robust, Flexible, Hydrophobic, and Multifunctional Pressure Sensor Based on an MXene/Aramid Nanofiber (ANF) Aerogel Film. *ACS Appl. Mater. Interfaces* **2022**, *14*, 47075-47088. https://doi.org/10.1021/ACSAMI.2C14094/ASSET/IMAGES/LARGE/AM2C14094_0011.JPEG.
32. Li, L.; Yuan, X.; Zhai, H.; Zhang, Y.; Ma, L.; Wei, Q.; Xu, Y.; Wang, G. Flexible and Ultrathin Graphene/Aramid Nanofiber Carbonizing Films with Nacre-like Structures for Heat-Conducting Electromagnetic Wave Shielding/Absorption. *ACS Appl. Mater. Interfaces* **2023**, *15*, 15872–15883. https://doi.org/10.1021/ACSAMI.3C00249/ASSET/IMAGES/LARGE/AM3C00249_0007.JPEG.
33. Hu, F.; Zeng, J.; Li, P.; Wang, T.; Li, J.; Wang, B.; Chen, K. Nacre-Inspired Strong Nanopapers of Aramid Nanofiber-Integrated Montmorillonite Nanoplates, Cellulose Nanofibrils, and Ag Nanowires for High-Performance Electrical Heaters. *J. Mater. Chem.* A. **2023**, *11*, 14126. *https://doi.org*/10.1039/d3ta02175k.
34. Hu, Y.; Yang, G.; Zhou, J.; Li, H.; Shi, L.; Xu, X.; Cheng, B.; Zhuang, X. Proton Donor-Regulated Mechanically Robust Aramid Nanofiber Aerogel Membranes for High-Temperature Thermal Insulation. *ACS Nano* **2022**, *16*, 5993. https://doi.org/10.1021/acsnano.1c11301.
35. Yin, Q.; Jia, H.; Liu, G.; Ji, Q.; Yin, Q.; Jia, H.; Liu, G.; Ji, Q. Tailoring the Mechanical Performance of Carbon Nanotubes Buckypaper by Aramid Nanofibers towards Robust and Compact Supercapacitor Electrode. *Adv. Funct. Mater.* **2022**, *32*, 2111177. https://doi.org/10.1002/ADFM.202111177.
36. Huang, L.; Xiao, G.; Wang, Y.; Li, H.; Zhou, Y.; Jiang, L.; Wang, J. Self-Exfoliation of Flake Graphite for Bioinspired Compositing with Aramid Nanofiber toward Integration of Mechanical and Thermoconductive Properties. *Nano-Micro Lett.* **2022**, *14*, 1–13. https://doi.org/10.1007/S40820-022-00919-0/FIGURES/6.
37. Wang, Z.G.; Jin, Y.F.; Hong, R.; Du, J.; Dai, K.; Zheng, G.Q.; Gao, J.; Xu, L.; Xu, J.Z.; Li, Z.M. Dual-Functional Thermal Management Materials for Highly Thermal Conduction and Effectively Heat Generation. *Compos. Part B Eng.* **2022**, *242*, 110084. https://doi.org/10.1016/J.COMPOSITESB.2022.110084.
38. Wang, X.; Cao, W.; Su, Z.; Zhao, K.; Dai, B.; Gao, G.; Zhao, J.; Zhao, K.; Wang, Z.; Sun, T.; et al. Fabrication of High Thermal Conductivity Nanodiamond / Aramid Nanofiber Composite Films with Superior Multifunctional Properties. **2023**. https://doi.org/10.1021/acsami.3c02574.
39. Zhou, J.; Thaiboonrod, S.; Fang, J.; Cao, S.; Miao, M.; Feng, X. In-Situ Growth of Polypyrrole on Aramid Nanofibers for Electromagnetic Interference Shielding Films with High Stability. *Nano Res.* **2022**, *15*, 8536–8545. https://doi.org/10.1007/s12274-022-4628-4.
40. Zeng, Z.; Chen, M.; Pei, Y.; Seyed Shahabadi, S.I.; Che, B.; Wang, P.; Lu, X. Ultralight and Flexible Polyurethane/Silver Nanowire Nanocomposites with Unidirectional Pores for Highly Effective Electromagnetic Shielding. *ACS Appl. Mater. Interfaces* **2017**, *9*, 32211–32219. https://doi.org/10.1021/ACSAMI.7B07643/ASSET/IMAGES/LARGE/AM-2017-07643Z_0006.JPEG.
41. Zhang, Y.; Lu, J.; Yu, J.; Jiang, X.; Wang, Y.; Chen, X.; Zhang, H.; Yang, L.; Yu, Y.; Qi, D. Large Scale Fabrication of Recyclable and Multifunctional Sandwich-Structured Electromagnetic Interference Shielding Films Based on Waste Nylon-6 Silk. *Mater. Today Phys.* **2023**, *36*, 101177. https://doi.org/10.1016/J.MTPHYS.2023.101177.
42. Chen, J.J.; Liu, S.L.; Wu, H. Bin; Sowade, E.; Baumann, R.R.; Wang, Y.; Gu, F.Q.; Liu, C.R.L.; Feng, Z.S. Structural Regulation of Silver Nanowires and Their Application in Flexible Electronic Thin Films. *Mater. Des.* **2018**, *154*, 266–274. https://doi.org/10.1016/J.MATDES.2018.05.018.
43. Ma, Z.; Kang, S.; Ma, J.; Shao, L.; Wei, A.; Liang, C.; Gu, J.; Yang, B.; Dong, D.; Wei, L.; et al. High-Performance and Rapid-Response Electrical Heaters Based on Ultraflexible, Heat-Resistant, and Mechanically Strong Aramid Nanofiber/Ag Nanowire Nanocomposite Papers. *ACS Nano* **2019**, *13*, 7578-7590. https://doi.org/10.1021/ACSNANO.9B00434/SUPPL_FILE/NN9B00434_SI_004.AVI.
44. Wang, Z.; Zhu, H.; Li, H.; Wang, Z.; Sun, M.; Yang, B.; Wang, Y.; Wang, L.; Xu, L. High-Strength Magnetic Hydrogels with Photoweldability Made by Stepwise Assembly of Magnetic-Nanoparticle-Integrated Aramid Nanofiber Composites. *ACS Nano* **2023**, *17*, 9622-9632. https://doi.org/10.1021/ACSNANO.3C03156.
45. Feng, L.; Wei, P.; Song, Q.; Zhang, J.; Fu, Q.; Jia, X.; Yang, J.; Shao, D.; Li, Y.; Wang, S.; et al. Superelastic, Highly Conductive, Superhydrophobic, and Powerful Electromagnetic Shielding Hybrid Aerogels Built from Orthogonal Graphene and Boron Nitride Nanoribbons. *ACS Nano* **2022**, *16*, 17049–17061. https://doi.org/10.1021/ACSNANO.2C07187/ASSET/IMAGES/LARGE/NN2C07187_0006.JPEG.

46. Deng, Z.; Jiang, P.; Wang, Z.; Xu, L.; Yu, Z.Z.; Zhang, H. Bin Scalable Production of Catecholamine-Densified MXene Coatings for Electromagnetic Shielding and Infrared Stealth. *Small* **2023**, 2304278. https://doi.org/10.1002/SMLL.202304278.